Analysis, Control, and Design of a Hybrid Grid-Connected Inverter for Renewable Energy Generation With Power Quality Conditioning

Lei Wang, Chi-Seng Lam, *Senior Member, IEEE*, and Man-Chung Wong, *Senior Member, IEEE*

***Abstract*—This paper proposes a new type dc/ac inverter named: hybrid-coupling grid-connected inverter (HGCI) for photovoltaic active power generation with power quality conditioning, which consists of a full-bridge three-phase dc/ac inverter coupling to the power grid in series with a thyristor-controlled *LC* filter. Compared with the conventional inductive-coupling grid-connected inverter (IGCI) and capacitive-coupling grid-connected inverter (CGCI), the proposed HGCI has distinct characteristics of wide operational range and low dc-link operating voltage. Based on these prominent characteristics, the system cost and operational cost can be reduced. Moreover, it can transfer the active power and compensate reactive power, unbalanced power, and harmonic power simultaneously. In this paper, the analysis of the structure, parameter design, and control method of the HGCI is proposed and presented. Finally, simulation and experimental results are provided to verify the effectiveness and performance of the proposed HGCI in comparison with the IGCI and CGCI.**

***Index Terms*—Active power, current harmonics, hybrid-coupling grid-connected inverter (HGCI), reactive power, thyristor-controlled *LC* (TCLC), unbalanced compensation.**

I. Introduction

THE modern power grids promise not only better electricity service and more reliable system but also environmental friendly energy. The solar energy as one of the most common renewable energy plays an important role in modern power grids due to its advantages of environmental friendliness, cost-efficiency, and mature technology. And, the global solar power capacity is predicted to reach 613 GW in 2020 from 285 GW in 2016, which is increasing rapidly. In order to transfer the solar energy to the loads or grids, researchers have been continuously improving the structure design and control methods of photovoltaic (PV) dc/ac inverters [1]–[14] based on the inductive-coupling grid-connected inverter (IGCI), in which the IGCI operating voltage should be higher than the power grid voltage or the dc-link voltage of the IGCI should be higher than the peak value of the power grid voltage. To meet this requirement, the possible inverter structures and characteristics for a PV energy generation system in a three-phase distribution power grid are shown in Fig. 1 and summarized as follows.

The basic structure characteristics of different dc/ac inverter topologies can be described as:

1) using a multilevel dc/ac inverter structure with each module supported by independent PV panels as energy source [5], [6];
2) using a line frequency voltage step-up transformer after the dc/ac inverter to step-up its operating voltage into the same power grid voltage level [7], [8];
3) step up the PV panel output voltage by using a dc–dc boost converter before the dc/ac inverter [9]–[11];
4) connecting many PV panels in series as the dc-link energy source for the dc/ac inverter [12]–[14].

However, due to the multilevel structure, *topology 1* [5], [6] requires many power switches and dc capacitors, which greatly increases the system cost and control complexity. By using the line frequency step-up transformers, *topology 2* [7], [8] can reduce the required power switches and dc capacitors. However, using the transformers still increases the size, weight, power loss, and cost of the system. Using a dc–dc boost converter to boost up the PV panel output voltage shown in *topology 3* [9]–[11] not only increases the control complexity but also decreases the system efficiency as compared with *topology 4*. The single-stage *topology 4* [12]–[14] will be the best choice among the four topologies because it can obtain the lowest cost and the highest efficiency, under the consideration of the same power transfer capability or number of PV panels. However, *topology 4* still requires large numbers of PV panels connected in series to support its high dc-link voltage requirement of IGCI ($>\sqrt{2}V_{L-L}$), which still occupies a large area and high costs.

Besides, from the China Meteorological Administration Wind and Solar Energy Resource Center, the average sunshine hour per year for the West part of China is less than 3600 h while that

Manuscript received May 5, 2017; revised July 27, 2017; accepted September 3, 2017. Date of publication September 17, 2017; date of current version April 20, 2018. This work was supported in part by the Science and Technology Development Fund, Macao SAR (FDCT) (025/2017/A1, 109/2013/A3) and in part by the Research Committee of the University of Macau (MYRG2015-00009-FST, MRG012/WMC/2015/FST, MYGR2017-00038-FST). Recommended for publication by Associate Editor Y. W. Li. *(Corresponding author: Chi-Seng Lam.)*

L. Wang is with the Department of Electrical and Computer Engineering, Faculty of Science and Technology, University of Macau, Macao, China.

C.-S. Lam is with the State Key Laboratory of Analog and Mixed Signal VLSI, University of Macau, Macao, China (e-mail: C.S.Lam@ieee.org; cslam@umac.mo).

M.-C. Wong is with the Department of Electrical and Computer Engineering, Faculty of Science and Technology and the State Key Laboratory of Analog and Mixed Signal VLSI, University of Macau, Macao, China.

Color versions of one or more of the figures in this paper are available online at http://ieeexplore.ieee.org.

Digital Object Identifier 10.1109/TPEL.2017.2753838

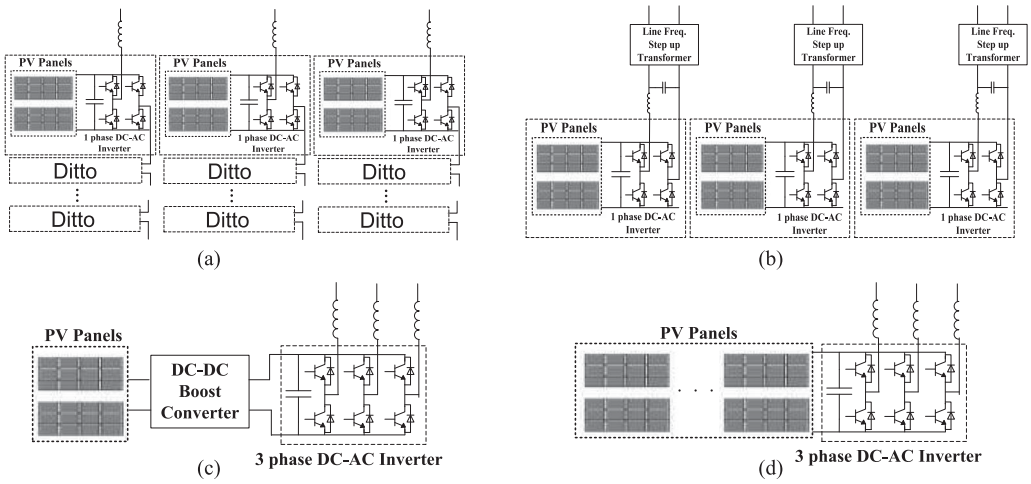

Fig. 1. Possible circuit topologies for a PV energy generation system [1]–[14] based on IGCI. (a) Topology 1. (b) Topology 2. (c) Topology 3. (d) Topology 4.

for the East part of China is even less than 2700 h, with one year of 8760 h [15]. That means the costly PV energy generation system does not operate almost 60% of the year if it just transfers the active power to the power grid only, which is not efficient and cost-effective. As a result, the PV generation system will work more cost-effectively if it can provide active power injection together with power quality conditioning (such as reactive power, current harmonic, and unbalanced power compensation) simultaneously. For example, the PV generation system can inject the active power and provide power quality conditioning in the daytime while it just compensates the power quality problem at night.

As the active power injection and power quality conditioning are fully supported by the inverter part only of the IGCI, this is the reason why the IGCI requires a high dc-link voltage, so as high-voltage rating switching devices. To reduce the required high dc-link voltage in *topology 4* and provide active power transfer and power quality conditioning functions simultaneously, the capacitive-coupling grid-connected inverters (CGCIs) have been proposed in [16] and [17]. For the CGCI structure, the dc/ac inverter is connected to the power grid via a series-connected *LC* filter. The coupling *LC* filter aims to compensate a fixed reactive power and a tuned harmonic current order and can provide a large fundamental voltage drop so as to significantly reduce the dc-link voltage requirement. With the low dc-link voltage characteristics, the CGCIs require less series-connected PV panels (mainly for active power injection and remaining current harmonics compensation), which offers the benefits of lower cost, lower operational loss, and higher reliability than the IGCI because it can use lower voltage rating switching devices and connect fewer PV panels in series. However, the large *LC* filter impedance of the CGCIs leads to a narrow energy conversion range. In addition, when the loading is capacitive or outside its operation range, the dc-link voltage is required to be higher than the power grid voltage, which loses its low dc-link voltage advantages.

A thyristor-controlled *LC*-coupled hybrid active power filter (TCLC-HAPF) is proposed for power quality compensation [18]–[23], in which it has distinct characteristics of wide compensation range and low active inverter capacity (no matter the loading is inductive or capacitive). However, the active power injection capability of this TCLC-HAPF has not been studied. This type of TCLC-HAPF is named as a hybrid grid-connected inverter (HGCI) for a PV energy generation system. In this paper, a single-stage, multitask HGCI structure is proposed for the PV energy generation system. The proposed HGCI can overcome the high dc-link voltage problem of the IGCIs and narrow energy conversion range of the CGCIs for both active power transfer and power quality conditioning simultaneously. Therefore, the HGCI requires low-voltage rating switching devices and operates with fewer PV panels connected in series. With the advantage of low dc-link voltage, the power loss can be reduced compared with the conventional IGCI. A comparison of IGCIs, CGCIs, and HGCIs is presented in Table I. Moreover, the proposed HGCI can

1) inject active power;
2) compensate reactive and harmonic power;
3) compensate the three-phase unbalanced power.

In this paper, the system configuration of the proposed HGCI is introduced in Section II. In Section III, the required inverter voltage of the HGCI is proposed in comparisons with the conventional IGCIs and the CGCIs. In Section IV, the parallel resonance prevention study of HGCI is provided. After that, the parameter design and control strategy of the HGCI are proposed in Sections V and VI. The simulation (see Section VII) and experimental results (see Section VIII) are provided to prove active power injection capability, wide power quality compensation range, and low dc-link voltage characteristics of the proposed HGCI. Finally, Section IX presents the conclusion.

II. Circuit Configuration of the Proposed HGCI

Fig. 2 shows the circuit configuration of the proposed HGCI, in which the subscript "x" stands for phases $a, b,$ and c in the following analysis. v_{sx} is the power grid source voltage; and $i_{sx}, i_{Lx},$ and i_{cx} are the source, load, and injecting currents, respectively. L_s is the transmission line impedance. The HGCI consists of a TCLC and an active inverter part.

TABLE I
COMPARISON OF IGCIS, CGCIS, AND HGCIS FOR A PV GENERATION SYSTEM WITH POWER QUALITY CONDITIONING

Inverter type	Active power Injection	Reactive power Comp.	Harmonic Comp.	Unbalanced power Comp.	DC-link voltage	Operate range	Power loss	Cost
IGCIs [12]–[14]	****	****	****	****	****	****	***	***
CGCIs [16], [17]	*	**	***	*	*	*	*	*
Proposed HGCI	***	****	****	****	*	****	*	**

Note: The shaded area means the undesirable characteristics.

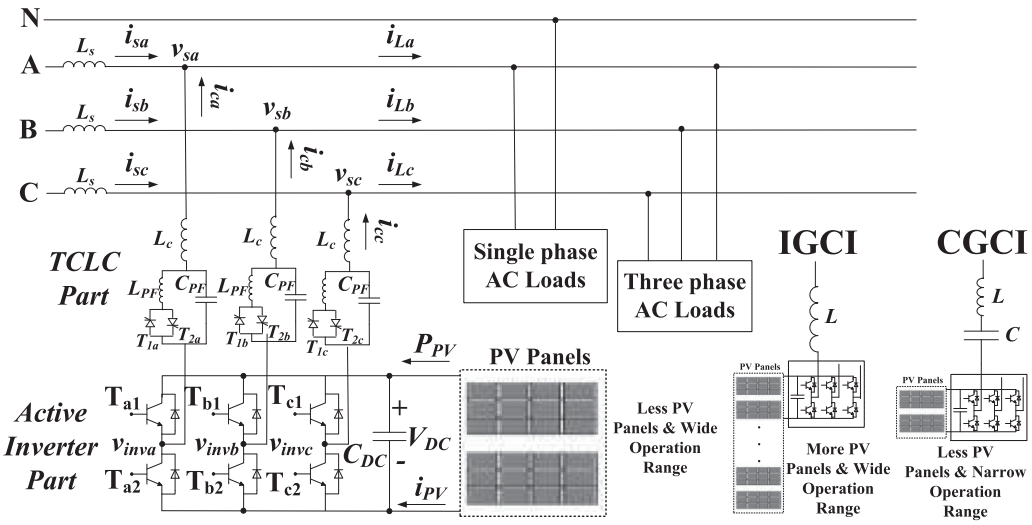

Fig. 2. Structure of the IGCI, CGCI, and the proposed HGCI for PV active power injection with power quality conditioning.

The TCLC part is composed of a coupling inductor L_c, a parallel capacitor $C_{\rm PF}$, and a thyristor-controlled reactor with $L_{\rm PF}$. The TCLC part provides a wide and continuous inductive and capacitive reactive power compensation range that is controlled by controlling the firing angles α_x of the thyristors. The active inverter part is composed of a dc/ac voltage source inverter (VSI) with a dc-link capacitor $C_{\rm DC}$ and a dc-link voltage $V_{\rm DC}$, and a small rating active inverter part is used to bear the PV active power injection, improve the performance of the TCLC part, and also compensate the current harmonics. Thus, it is possible to connect fewer PV panels in series in comparison with the IGCI case for active power transfer and power quality conditioning. The HGCI requires low-voltage rating switching devices of the active inverter part, and the cost and switching loss of the thyristor are much lower than those switching devices. Therefore, the initial cost and operational loss of the HGCI are less than the IGCI. In addition, the coupling components of the conventional IGCI and CGCI are also presented in Fig. 2 for comparison.

III. CHARACTERISTIC STUDY OF THE IGCI, CGCI, AND THE PROPOSED HGCI

As mentioned in the previous section, the grid-connected inverters are used to inject active power and reactive power to the grid at the fundamental frequency when they are used to integrate the PV energy generation system with power quality conditioning. The current injected to the grid by the VSI can be expressed as

$$I_{cxf} = I_{cxfp} + j \cdot I_{cxfq} \tag{1}$$

where the subscript "f" represents the fundamental frequency component, and I_{cxfp} is the fundamental active current that is injected or absorbed from the grid. I_{cxfq} is the fundamental reactive current that is injected or absorbed to the grid. The fundamental output voltage of the VSI of the HGCI is given as

$$\begin{aligned} V_{\rm invxf} &= \vec{V}_{sxf} + {\rm X}_{\rm TCLC} \cdot \vec{I}_{cxf} \\ &= \vec{V}_{sxf} + {\rm X}_{\rm TCLC}(\alpha_x) \cdot (\vec{I}_{cxpf} + j\vec{I}_{cxqf}). \end{aligned} \tag{2}$$

In (2), the TCLC part impedance $X_{\rm TCLC}(\alpha_x)$ of the HGCI can be expressed as

$$\begin{aligned} X_{\rm TCLC}(\alpha_x) &= \frac{X_{\rm TCR}(\alpha_x) X_{C_{\rm PF}}}{X_{C_{\rm PF}} - X_{\rm TCR}(\alpha_x)} + X_{L_c} \\ &= \frac{\pi X_{L_{\rm PF}} X_{C_{\rm PF}}}{X_{C_{\rm PF}}(2\pi - 2\alpha_x + \sin 2\alpha_x) - \pi X_{L_{\rm PF}}} + X_{L_c} \end{aligned} \tag{3}$$

where X_{Lc}, $X_{\rm LPF}$, and $X_{\rm CPF}$ are the fundamental impedances of $L_c, L_{\rm PF},$ and $C_{\rm PF}$, respectively. In (3), it is shown that the TCLC part impedance is controlled by the firing angle α_x. And the minimum inductive and capacitive impedances (absolute value) of the TCLC part can be obtained by substituting the firing angles $\alpha_x = 90^\circ$ and 180° into (3), respectively. In the following discussion, the minimum value for impedance stands

for its absolute value. The minimum inductive ($X_{\mathrm{ind(min)}} > 0$) and capacitive ($X_{\mathrm{Cap(min)}} < 0$) TCLC part impedances can be expressed as

$$X_{\mathrm{Ind(min)}}(\alpha_x = 90^\circ) = \frac{X_{L_{\mathrm{PF}}} X_{C_{\mathrm{PF}}}}{X_{C_{\mathrm{PF}}} - X_{L_{\mathrm{PF}}}} + X_{L_c} \tag{4}$$

$$X_{\mathrm{Cap(min)}}(\alpha_x = 180^\circ) = -X_{C_{\mathrm{PF}}} + X_{L_c}. \tag{5}$$

Based on (1)–(3), the injected active power and reactive power by the HGCI can be expressed as

$$\begin{aligned} S_{cxf} &= \vec{V}_{sxf}\vec{I}^{*}_{cxf} = \vec{V}_{sxf} \cdot \left(\frac{\vec{V}_{\mathrm{inv}xf} - \vec{V}_{sxf}}{jX_{\mathrm{TCLC}}(\alpha_x)}\right)^{*} \\ &= V_{sxf} \cdot \left(\frac{(V_{\mathrm{inv}xf}\cos\delta + jV_{\mathrm{inv}xf}\sin\delta) - V_{sxf}}{jX_{\mathrm{TCLC}}(\alpha_x)}\right)^{*} \\ &= V_{sxf} \cdot \left(\frac{V_{\mathrm{inv}xf}\sin\delta}{X_{\mathrm{TCLC}}(\alpha_x)} + j\frac{\vec{V}_{\mathrm{inv}xf}\cos\delta - \vec{V}_{sxf}}{X_{\mathrm{TCLC}}(\alpha_x)}\right) \\ &= \frac{V_{sxf}V_{\mathrm{inv}xf}\sin\delta}{X_{\mathrm{TCLC}}(\alpha_x)} + j\left(\frac{V_{sxf}V_{\mathrm{inv}xf}\cos\delta}{X_{\mathrm{TCLC}}(\alpha_x)} - \frac{V_{sxf}^2}{X_{\mathrm{TCLC}}(\alpha_x)}\right) \\ &= P_{cxf} + \mathrm{j}Q_{cxf} \end{aligned} \tag{6}$$

where * is the conjugate value, and δ is the angle between the inverter voltage $V_{\mathrm{inv}xf}$ and the source voltage V_{sxf}. Based on (6), the ratio of $V_{\mathrm{inv}f}/V_{sxf}$ can be expressed as

$$\frac{V_{\mathrm{inv}xf}}{V_{sxf}} = \sqrt{\left(\frac{P_{cxf}}{S_{\mathrm{base}H}}\right)^2 + \left(\frac{Q_{cxf}}{S_{\mathrm{base}H}} - 1\right)^2} \tag{7}$$

where $S_{\mathrm{base}H}$ is the base power of the HGCI, which can be expressed as

$$S_{\mathrm{base}H} = \frac{V_{sxf}^2}{X_{\mathrm{TCLC}}(\alpha_x)}. \tag{8}$$

In (8), $X_{\mathrm{TCLC}}(\alpha_x)$ is controlled by the firing angle which can be obtained from (3). In other words, the $S_{\mathrm{base}H}$ is controlled by the firing angle of the thyristors. In order to get the minimum ratio of $V_{\mathrm{inv}f}/V_{sxf}$ in (7), so as to achieve the minimum dc-link voltage requirement for the HGCI, the optimal $S_{\mathrm{base}H}$ can be calculated by taking the derivative of $V_{\mathrm{inv}f}/V_{sxf}$ with regard to $S_{\mathrm{base}H}$ to zero

$$\frac{\partial\left(V_{\mathrm{inv}xf}/V_{sxf}\right)}{\partial S_{\mathrm{base}H}} = 0, \quad S_{\mathrm{base}H} = \frac{P_{cxf}^2 + Q_{cxf}^2}{Q_{cxf}}. \tag{9}$$

If the deduced $S_{\mathrm{base}H}$ in (9) is within the range $S_{\mathrm{base}H} \in [V_{sxf}^2/X_{\mathrm{TCLC}}(\alpha_x = 180^\circ), V_{sxf}^2/X_{\mathrm{TCLC}}(\alpha_x = 90^\circ)]$, the ratio of $V_{\mathrm{inv}f}/V_{sxf}$ can be calculated by substituting $S_{\mathrm{base}H}$ in (9) into (7). Otherwise, the ratio of $V_{\mathrm{inv}f}/V_{sxf}$ can be calculated with $S_{\mathrm{base}H} = V_{sxf}^2/X_{\mathrm{TCLC}}(\alpha_x = 180^\circ)$ or $S_{\mathrm{base}H} = V_{sxf}^2/X_{\mathrm{TCLC}}(\alpha_x = 90^\circ)$. Compared with the HGCI, the coupling impedances for the IGCIs and CGCIs are shown in Fig. 2, which are fixed as X_L and $X_L - X_C$. The base power of IGCI and CGCI can be expressed as

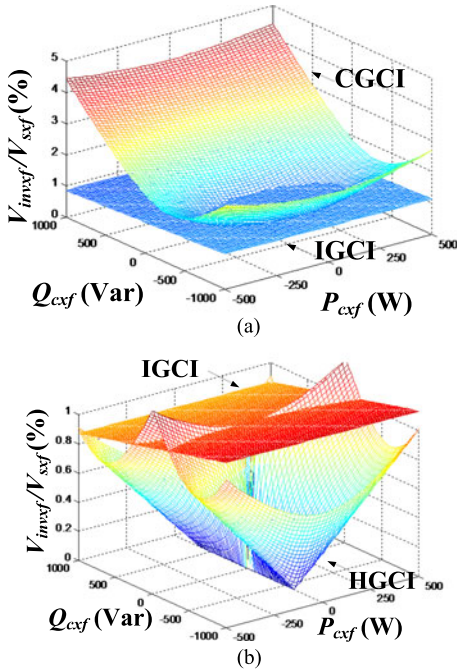

Fig. 3. Ratio of $V_{\mathrm{inv}f}/V_{sxf}$ in terms of P_{cxf} and Q_{cxf}: (a) IGCI and CGCI, and (b) IGCI and the proposed HGCI.

$$S_{\mathrm{Base}I} = \frac{V_{sxf}^2}{2\pi fL} \tag{10}$$

$$S_{\mathrm{Base}C} = \frac{V_{sxf}^2}{2\pi fL - \frac{1}{2\pi fC}}. \tag{11}$$

From (10) and (11), the base power of the IGCI and CGCI is a fixed value. By substituting (10) and (11) into (7) ($S_{\mathrm{base}H} = S_{\mathrm{base}I}$ and $S_{\mathrm{base}H} = S_{\mathrm{base}C}$), the ratio of $V_{\mathrm{inv}f}/V_{sxf}$ in terms of P_{cxf} and Q_{cxf} can be plotted as Fig. 3(a) and (b). The plots of the IGCI in Fig. 3(a) and (b) are the same.

For IGCI shown in Fig. 3(a) and (b), $V_{\mathrm{inv}xf}/V_{sxf} > 1$ when the loading is inductive. In contrast, the required $V_{\mathrm{inv}xf}/V_{sxf}$ is slightly smaller than 1 when the required reactive power is capacitive. Actually, the $V_{\mathrm{inv}xf}/V_{sxf}$ is close to one due to the small value of the coupling inductor L.

For CGCI shown in Fig. 3(a), it is shown that $V_{\mathrm{inv}xf}/V_{sxf}$ is lower than 1 under a small inductive reactive power area. In contrast, the ratio of $V_{\mathrm{inv}xf}/V_{sxf}$ increases rapidly when Q_{cxf} is moving away from $S_{\mathrm{base}C}$.

For the proposed HGCI shown in Fig. 3(b), if the deduced $S_{\mathrm{base}H}$ in (9) is within the range $S_{\mathrm{base}H} \in [V_{sxf}^2/X_{\mathrm{TCLC}}(\alpha_x = 180^\circ), V_{sxf}^2/X_{\mathrm{TCLC}}(\alpha_x = 90^\circ)]$, the ratio of $V_{\mathrm{inv}f}/V_{sxf}$ can always be smaller or equal to 1. This phenomenon can be proved mathematically by substituting (9) into (7)

$$\begin{aligned} \frac{V_{\mathrm{inv}xf}}{V_{sxf}} &= \sqrt{\frac{P_{cxf}^2}{S_{\mathrm{base}H}} + \left(\frac{Q_{cxf}}{S_{\mathrm{base}H}} - 1\right)^2} \\ &= \sqrt{\frac{P_{cxf}^4 + P_{cxf}^2 Q_{cxf}^2}{\left(P_{cxf}^2 + Q_{cxf}^2\right)^2}} \le 1 \end{aligned} \tag{12}$$

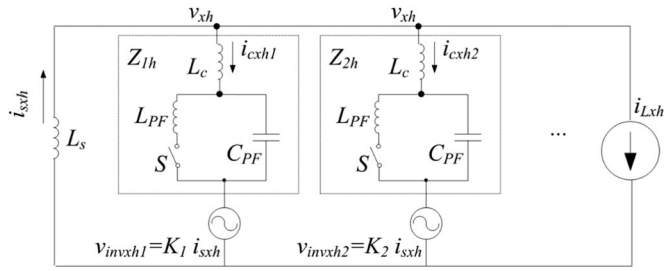

Fig. 4. Harmonic equivalent circuit model of parallel HGCIs due to i_{Lxh}.

where $S_{\mathrm{base}H}$ is designed to be

$$S_{\mathrm{base}H} = \frac{V_{sxf}^2}{X_{\mathrm{TCLC}}(\alpha_x)} = \frac{P_{cxf}^2 + Q_{cxf}^2}{Q_{cxf}}. \tag{13}$$

The basic function of the HGCI at the fundamental frequency is to inject P_{cxf} and compensate Q_{cxf} to the power grid simultaneously in the daytime; and it provides Q_{cxf} compensation at night, which makes the PV generation system to work more cost-effectively instead of just injecting active power during sunshine hours in the daytime. Another desirable function of the HGCI is that $V_{\mathrm{inv}f}/V_{sxf}$ can be as small as zero when it provides Q_{cxf} compensation only at nighttime. This phenomenon can be observed from Fig. 3(b) (with $P_{cxf} = 0$), and also can be proved by using (12) as

$$\frac{V_{\mathrm{inv}xf}}{V_{sxf}} = \lim_{P_{cxf}\to 0} \sqrt{\frac{P_{cxf}^4 + P_{cxf}^2 Q_{cxf}^2}{(P_{cxf}^4 + 2P_{cxf}^2 Q_{cxf}^2) + Q_{cxf}^4}} = 0. \tag{14}$$

Compared with the IGCI and CGCI, the HGCI requires the lowest required fundamental inverter voltage $V_{\mathrm{inv}f}$ to inject P_{cxf} and compensate Q_{cxf} to the power grid simultaneously in the daytime or compensate Q_{cxf} at the nighttime. As the fundamental inverter voltage usually dominates the design of the dc-link voltage of the dc/ac VSI, the HGCI can obtain the lowest dc-link voltage requirement among the IGCI and CGCI.

IV. Parallel Resonance Prevention of HGCI

The pure TCLC part operation may cause the resonance problem, but the active inverter part of HGCI can help to alleviate the resonance problem. The TCLC part is controlled by thyristors which can be modeled as a switch. When the switch is turned OFF, the TCLC part is L_c in series with C_{PF} (LC-mode). When the switch is turned ON, the TCLC part is L_c in series with the paralleled combination of L_{PF} and C_{PF} (LCL-mode).

Fig. 4 shows its equivalent circuit model of parallel HGCIs due to load harmonic current i_{Lxh}. The subscript "h" denotes the harmonic component. In the harmonic model shown in Fig. 4, the inverters of the parallel HGCIs can be treated as a current-controlled voltage source, which can be expressed as

$$v_{\mathrm{inv}xh1} = K_1 \cdot i_{sxh}, \quad v_{\mathrm{inv}xh2} = K_2 \cdot i_{sxh} \tag{15}$$

where i_{sxh} is the source harmonic current, and K_1 and K_2 are the control gains which depend on the inverter part of the parallel HGCIs. Referring to Fig. 4, the ratio of i_{sxh} and i_{Lxh} under both *LC-mode* and *LCL-mode* can be expressed as

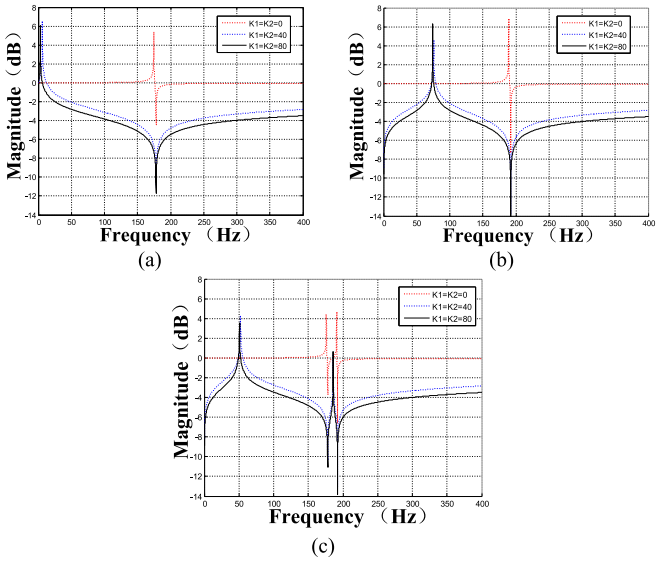

Fig. 5. Bode diagrams of parallel HGCIs under resonance analysis: (a) both *LC* modes, (b) both *LCL* modes, and (c) one *LC* mode and one *LCL* mode.

$$K_{sh} = \frac{i_{sxh}}{i_{Lxh}} = \frac{Z_{1h}//Z_{2h}}{Z_{sh} + K_1 + K_2 + Z_{1h}//Z_{2h}} \tag{16}$$

where Z_{sh} is the harmonic impedance of system L_s. Z_{1h} and Z_{2h} are harmonic impedances of the TCLC part of the parallel HGCIs. $K_1 = 0$ and $K_2 = 0$ for the operation of pure TCLC part (no inverter) of the parallel HGCIs while $K_1 > 0$ and $K_2 > 0$ for the operation of the parallel HGCIs.

With the help of (16) and the bode diagrams shown in Fig. 5, the possible parallel resonance problem of the parallel HGCIs can be analyzed. The existence of K_1 and K_2 can eliminate the original resonance condition of the pure TCLC part operation at $|Z_{sh} + Z_{1h}//Z_{2h}| \approx 0$ in (16), thus playing a similar damping role as Z_{sh}. Hence, the pole of the transfer function shifts to a lower frequency. The $K_1 = K_2 = 0$ plot in Fig. 5 describes the corresponding transfer function with only pure TCLC part operation. The $K_1 = K_2 = 40$ and $K_1 = K_2 = 80$ plots indicate the transfer function with the parallel HGCIs operation. The amplitude frequency response shows a damping characteristic due to the load harmonic current.

V. Parameter Design of HGCI

The TCLC part of the proposed HGCI is designed based on the consideration of the injection of P_{cxf} and the compensation Q_{cxf} range (for L_{PF} and C_{PF}) and the limitation of the high-frequency switching current ripple (for L_c).

A. Design of C_{PF} and L_{PF}

The purpose of the TCLC part is to provide the optimum based power $S_{\mathrm{Base}H}$ as in (9). In (9), when the $X_{\mathrm{TCLC}}(\alpha_x) = X_{\mathrm{Cap(min)}}(\alpha_x = 180^\circ)$ or $X_{\mathrm{TCLC}}(\alpha_x) = X_{\mathrm{Ind(min)}}(\alpha_x = 90^\circ)$, the TCLC part provides the maximum capacitive or inductive compensating reactive power

$Q_{cxf(\mathrm{MaxCap})} > 0$ and $Q_{cxf(\mathrm{MaxInd})} < 0$, respectively. Therefore, $S_{\mathrm{Base}H(\mathrm{MaxCap})}$ and $S_{\mathrm{Base}H(\mathrm{MaxCap})}$ via (13) can be expressed as

$$S_{\mathrm{Base}H(\mathrm{MaxCap})} = \frac{P_{cxf(\mathrm{Max})}^2 + Q_{cxf(\mathrm{MaxCap})}^2}{Q_{cxf(\mathrm{MaxCap})}} = \frac{V_{sxf}^2}{X_{\mathrm{Cap(min)}}(\alpha_x = 180°)} = -\frac{V_{sxf}^2}{X_{C_{\mathrm{PF}}} - X_{L_c}} \tag{17}$$

$$S_{\mathrm{Base}H(\mathrm{MaxInd})} = \frac{P_{cxf(\mathrm{Max})}^2 + Q_{cxf(\mathrm{MaxInd})}^2}{Q_{cxf(\mathrm{MaxInd})}} = \frac{V_{sxf}^2}{X_{\mathrm{Ind(min)}}(\alpha_x = 90°)} = \frac{V_{sxf}^2}{\frac{X_{L_{\mathrm{PF}}} X_{C_{\mathrm{PF}}}}{X_{C_{\mathrm{PF}}} - X_{L_{\mathrm{PF}}}} + X_{L_c}} \tag{18}$$

where the minimum inductive impedance $X_{\mathrm{Ind(min)}}$ and the capacitive impedance $X_{\mathrm{Cap(min)}}$ are obtained from (4) and (5), respectively. Based on (17) and (18), the parallel capacitor C_{PF} and inductor L_{PF} can be designed as, (19) and (20) shown at the bottom of this page, where $P_{cxf(\mathrm{Max})}$ is the designed maximum injected active power, and $Q_{cxf(\mathrm{MaxCap})}$ and $Q_{cxf(\mathrm{MaxInd})}$ are the designed maximum compensated inductive and capacitive reactive power. ω is the fundamental angular frequency and V_{sxf} is the root-mean-square source voltage.

B. Design of L_c

A coupling inductor L_c is used to limit the high-frequency switching current ripple. According to [17], the impedance of the coupling L_c can be designed to be larger or equal to 5% of the impedance of the coupling capacitor C_{PF} as

$$L_c \geq \frac{0.05}{\omega^2 \cdot C_{\mathrm{PF}}} \tag{21}$$

where C_{PF} is the TCLC part capacitor which can be found from (19).

VI. Control Strategy of HGCI

In this part, the control strategy for the HGCI is proposed by coordinating the control of the TCLC part and the active inverter part, so that the two parts can complement each other's disadvantages and the overall performance of the HGCI can be improved. And, the control block diagram of the HGCI is shown in Fig. 6.

The control strategy of the HGCI is separated into two parts for discussion: A) TCLC part control and B) active inverter part control.

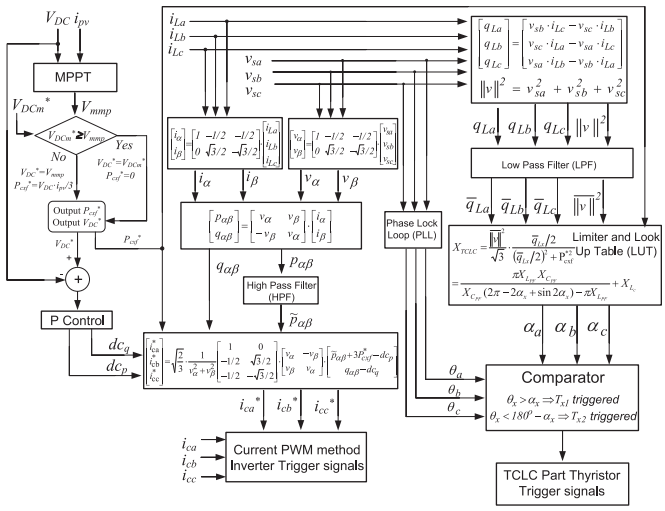

Fig. 6. Control block diagram of the proposed HGCI.

A. TCLC Part Control

The TCLC part control is based on the instantaneous *pq* theory [17]. The TCLC part is mainly used to instantaneously inject the reference $P_{cxf}{}^*$ (from PV source) and compensate the load reactive power $Q_{cxf} = Q_{Lxf} \approx \bar{q}_{Lx}/2$. Referring to (13), to calculate X_{TCLC} in real time, the expression of X_{TCLC} can be expressed in terms of instantaneous values as

$$X_{\mathrm{TCLC}}(\alpha_x) = \frac{Q_{cxf} V_{sxf}^2}{P_{cxf}^2 + Q_{cxf}^2} = \frac{\overline{\|v\|}^2}{\sqrt{3}} \times \frac{\bar{q}_{Lx}/2}{\left(\bar{q}_{Lx}/2\right)^2 + P_{cxf}^{*2}} \tag{22}$$

where $\|v\|$ is the norm of the three-phase instantaneous source voltage v_{sx} and $\bar{q}_{Lx}$ is the dc component of the load reactive power. The expression of $\|v\|$ and $\bar{q}_{Lx}$ with low-pass filters can be obtained by [24]

$$\|v\| = \sqrt{v_{sa}^2 + v_{sb}^2 + v_{sc}^2} \tag{23}$$

$$\begin{bmatrix} q_{La} \\ q_{Lb} \\ q_{Lc} \end{bmatrix} = \begin{bmatrix} v_{sb} \cdot i_{Lc} - v_{sc} \cdot i_{Lb} \\ v_{sc} \cdot i_{La} - v_{sa} \cdot i_{Lc} \\ v_{sa} \cdot i_{Lb} - v_{sb} \cdot i_{La} \end{bmatrix}. \tag{24}$$

In (23) and (24), v_{sx} and q_{Lx} are the instantaneous load voltage and the load reactive power, respectively. By comparing the calculated X_{TCLC} in (22) and X_{TCLC} expression in (3), the firing angle α_x can be determined. Because (3) is complicated, a look-up table between the firing angle α_x and X_{TCLC} is installed inside the controller. The trigger signals to control the

$$C_{\mathrm{PF}} = \frac{P_{cxf(\mathrm{Max})}^2 + Q_{cxf(\mathrm{MaxCap})}^2}{\omega^2 L_c \left(P_{cxf(\mathrm{Max})}^2 + Q_{cxf(\mathrm{MaxCap})}^2\right) - \omega V_{sxf}^2 \cdot Q_{cxf(\mathrm{MaxCap})}} \tag{19}$$

$$L_{\mathrm{PF}} = \frac{V_{sxf}^2 Q_{cxf(\mathrm{MaxInd})} - \omega L_c \left(P_{cxf(\mathrm{Max})}^2 + Q_{cxf(\mathrm{MaxInd})}^2\right)}{\omega \left(P_{cxf(\mathrm{Max})}^2 + Q_{cxf(\mathrm{MaxInd})}^2\right) - \omega^3 L_c C_{\mathrm{PF}} \left(P_{cxf(\mathrm{Max})}^2 + Q_{cxf(\mathrm{MaxInd})}^2\right) + \omega^2 V_{sxf}^2 C_{\mathrm{PF}} Q_{cxf(\mathrm{MaxInd})}} \tag{20}$$

TCLC part can then be generated by comparing the firing angle α_x with θ_x, which is the phase angle of the source voltage v_{sx}. θ_x can be obtained by using a phase lock loop.

B. Active Inverter Part Control

The active inverter part is explained into two parts. In Section VI-B1, the dc-link voltage control with the maximum power point tracking (MPPT) is proposed and discussed. In Section VI-B2, the reference current calculation is introduced.

1) DC-Link Voltage Control With the MPPT: Because the PV power output is usually affected by the weather, the commonly used MPPT leads to active power changing in time, which can affect the active inverter part dc-link voltage $V_{\rm DC}$ of the HGCI.

For the HGCI system, the TCLC part is used to compensate reactive power and unbalanced power. And, the active inverter part with dc-link voltage $V_{\rm DC}$ is used to compensate harmonic power and inject active power (P_{cxf}). Therefore, a minimum dc-link voltage reference ${V_{\rm DC}}_m{}^*$ is still required and can be calculated based on harmonic current compensation when the reference active power injection ${P_{cxf}}^* = 0$. ${V_{\rm DC}}_m{}^*$ can be expressed as

$$\begin{aligned} V^*_{{\rm DC}m} &= \max\left(\sqrt{6}\cdot V_{{\rm inv}ah},\ \sqrt{6}\cdot V_{{\rm inv}bh},\ \sqrt{6}\cdot V_{{\rm inv}ch}\right) \\ &= \max\left(\sqrt{6}\sqrt{\sum_{n=2}^{\infty}\left(X_{an}\cdot I_{Lan}\right)^2},\ \sqrt{6}\sqrt{\sum_{n=2}^{\infty}\left(X_{bn}\cdot I_{Lbn}\right)^2},\right. \\ &\quad \left.\sqrt{6}\sqrt{\sum_{n=2}^{\infty}\left(X_{cn}\cdot I_{Lcn}\right)^2}\right) \end{aligned} \tag{25}$$

where I_{Lxn} is the load harmonic current at each harmonic order n, and X_{xn} is the harmonic impedance of the TCLC part, which can be expressed as

$$\begin{aligned} |X_{xn}(\alpha)| = \Bigg| &\frac{\pi(n\omega L_{\rm PF})}{(2\pi - 2\alpha + \sin 2\alpha) - \pi(n\omega)^2\cdot L_{\rm PF}C_{\rm PF}} \\ &+ n\omega L_c\Bigg| \end{aligned} \tag{26}$$

Once the MPPT method leads to the PV output voltage $V_{\rm mmp}$ lower than its ${V_{\rm DC}}_m{}^*$, the reference dc-link voltage ${V_{\rm DC}}^*$ will be equal to ${V_{\rm DC}}_m{}^*$. In this situation, the HGCI is controlled to compensate reactive power, unbalanced power, and harmonics power only (without active power injection ${P_{cxf}}^* = 0$), which is similar as its targeted operation at night. The HGCI can resume its active power injection once the MPPT-controlled PV output voltage $V_{\rm mmp}$ is higher than its ${V_{\rm DC}}_m{}^*$. When $V_{\rm mmp} > {V_{\rm DC}}_m{}^*$, ${V_{\rm DC}}^* = V_{\rm mmp}$, the HGCI with the PV power is used to inject active power $({P_{cxf}}^* = V_{\rm DC}\cdot i_{\rm PV}/3)$ and compensate reactive power, unbalanced power, and harmonics power simultaneously.

The HGCI can effectively control the dc-link voltage by feedback the dc voltage controlled signal. According to dc-link voltage control study in [26]–[28], the feedback signals use both reactive and active components (dc_q, dc_p) with proportional (*P*) control:

$$dc_q = -k_q\cdot(V^*_{\rm DC} - V_{\rm DC}) \tag{27}$$

$$dc_p = k_p\cdot(V^*_{\rm DC} - V_{\rm DC}) \tag{28}$$

where k_q and k_p are the proportional gains of the dc-link voltage controller. dc_q and dc_p are the dc control signals related to the reactive and active current components. dc_q aims to step change the dc-link voltage under insufficient dc-link voltage, which can be effectively applied for start-up process while dc_p aims to maintain the dc-link voltage due to the system loss.

2) Reference Current Calculation: In the proposed control strategy, the instantaneous active and reactive power theory method [25] is implemented for the active inverter part to inject active power $(3{P_{cxf}}^* = V_{\rm DC}\cdot i_{\rm PV})$ and compensate reactive power $(\bar{q}_{\alpha\beta})$ and harmonic current ($\tilde{p}_{\alpha\beta}$ and $\tilde{q}_{\alpha\beta}$). Specifically, the active inverter part is used to limit the compensating current i_{cx} to track its reference value ${i_{cx}}^*$. ${i_{cx}}^*$ can be calculated as

$$\begin{aligned} \begin{bmatrix} i^*_{ca}\\ i^*_{cb}\\ i^*_{cc}\end{bmatrix} &= \sqrt{\frac{2}{3}}\cdot\frac{1}{v_\alpha^2+v_\beta^2}\begin{bmatrix}1 & 0\\ -1/2 & \sqrt{3}/2\\ -1/2 & -\sqrt{3}/2\end{bmatrix}\cdot\begin{bmatrix}v_\alpha & -v_\beta\\ v_\beta & v_\alpha\end{bmatrix} \\ &\quad\cdot\begin{bmatrix}\tilde{p}_{\alpha\beta} + 3{P_{cxf}}^* - dc_p\\ q_{\alpha\beta} - dc_q\end{bmatrix} \end{aligned} \tag{29}$$

where $V_{\rm DC}$ and $i_{\rm PV}$ are the measured dc-link voltage and PV current, and dc_q and dc_p are the dc control signals related to the reactive and active current components, which can be obtained from (27) and (28). $p_{\alpha\beta}$ and $q_{\alpha\beta}$ are the instantaneous active and reactive powers of the loading which include dc components $\bar{p}_{\alpha\beta}$ and $\bar{q}_{\alpha\beta}$, and ac components $\tilde{p}_{\alpha\beta}$ and $\tilde{q}_{\alpha\beta}$. $\bar{p}_{\alpha\beta}$ and $\bar{q}_{\alpha\beta}$ contain the fundamental active and reactive current components, respectively, while $\tilde{p}_{\alpha\beta}$ and $\tilde{q}_{\alpha\beta}$ contain harmonic currents and negative sequence components. $\tilde{p}_{\alpha\beta}$ is obtained by passing $p_{\alpha\beta}$ through a high-pass filter. $p_{\alpha\beta}$ and $q_{\alpha\beta}$ can be obtained as

$$\begin{bmatrix}p_{\alpha\beta}\\ q_{\alpha\beta}\end{bmatrix} = \begin{bmatrix}v_\alpha & v_\beta\\ -v_\beta & v_\alpha\end{bmatrix}\cdot\begin{bmatrix}i_\alpha\\ i_\beta\end{bmatrix}. \tag{30}$$

In (29) and (30), the voltages (v_α and v_β) and currents (i_α and i_β) in the $\alpha-\beta$ plane are transformed from $a-b-c$

TABLE II
SIMULATION AND EXPERIMENTAL PARAMETERS FOR THE IGCI, CGCI, AND HGCI

	Parameters	Physical values
System parameters	V_{sx}, f, L_s	110 V, 50 Hz,0.1 mH
IGCI	L	5 mH (0.14 p.u.)
CGCI	L, C	5 mH (0.14 p.u.), 80 μF (3.6 p.u.)
HGCI	$L_c, L_{\rm PF}, C_{\rm PF}$	5 mH (0.14 p.u.), 30 mH (0.87 p.u.), 160 μF (1.8 p.u.)

TABLE III
SIMULATION RESULTS FOR DIFFERENT LOADS COMPENSATION BEFORE AND AFTER THE IGCI, CGCI, AND HGCI COMPENSATION

			I_{sx} (A)	Q_{sx} (var)	P_{sx} (W)	PF	THD_{isx} (%)	V_{DC} (V)
Linear load ($P_{cxf}{}^* = 200$ W)	Before		7.6	540	630	0.76	0.1	–
	IGCI Comp.		4.2	8	468	1.00	2.1	300
	CGCI Comp.		4.0	18	433	1.00	2.3	300
	HGCI Comp.		4.1	15	443	1.00	2.5	100
Nonlinear load ($P_{cxf}{}^* = 200$ W)	Before		9.3	540	864	0.85	16.2	–
	IGCI Comp.		7.3	10	700	1.00	10.7	300
	IGCI Comp.		6.4	11	680	1.00	3.7	400
	CGCI Comp.		6.2	20	650	1.00	2.4	300
	HGCI Comp.		6.2	28	674	1.00	4.3	100
Unbalanced loads ($P_{cxf}{}^* = 100$ W)	Before Comp.	A	6.2	486	457	0.68	27.4	–
		B	6.2	280	608	0.91	27.3	
		C	8.1	508	708	0.81	20.7	
	After HGCI Comp.	A	4.6	1	498	1.00	3.0	100
		B	4.6	10	498	1.00	4.7	
		C	4.6	5	499	1.00	4.6	

frames by

$$\begin{bmatrix} v_\alpha \\ v_\beta \end{bmatrix} = \begin{bmatrix} 1 & -1/2 & -1/2 \\ 0 & \sqrt{3}/2 & -\sqrt{3}/2 \end{bmatrix} \cdot \begin{bmatrix} v_{sa} \\ v_{sb} \\ v_{sc} \end{bmatrix} \text{ and}$$

$$\begin{bmatrix} i_\alpha \\ i_\beta \end{bmatrix} = \begin{bmatrix} 1 & -1/2 & -1/2 \\ 0 & \sqrt{3}/2 & -\sqrt{3}/2 \end{bmatrix} \cdot \begin{bmatrix} i_{La} \\ i_{Lb} \\ i_{Lc} \end{bmatrix} \tag{31}$$

where v_{sx} and i_{Lx} are source voltage and load current signals. Finally, by comparing compensating current i_{cx} with the reference value $i_{cx}{}^*$ through the hysteresis pulse-width modulation (PWM) control method, the triggers for active inverter part can be generated.

VII. SIMULATION STUDY OF HGCI

In this section, simulation case studies are provided to verify the proposed HGCI can perform active power injection, reactive power, and harmonic current compensation under different loading conditions (balanced/unbalanced) in comparison with the IGCI and CGCI. With the based value of $V_{\mathrm{base}} = 110\,\mathrm{V}$, $I_{\mathrm{base}} = 10\,\mathrm{A}$, and $X_{\mathrm{base}} = V_{\mathrm{base}}/I_{\mathrm{base}} = 11\,\Omega$, Table II presents the parameters used in the both simulations and experiments. The values of L_{PF} and C_{PF} in HGCI are designed based on the reactive power/current compensation and active power injection range. A small rating HGCI (110 V–10 A) experimental prototype is built in the laboratory for testing purpose. And, L_{PF} and C_{PF} are selected to be 30 mH and 160 μF due to the small rating HGCI. For practical industrial application with wider reactive power compensation range and active power injection, a much smaller L_{PF} value can be designed. Table III summarizes all the above-mentioned simulation results by using the IGCI, CGCI, and HGCI. The comparative performances of IGCI, CGCI, and HGCI are given in Section VII-A. And, the electromagnetic interference (EMI) impact of the HGCI is provided in Section VII-B. The HGCI for unbalanced loads compensation is presented in Section VII-C. Finally, the HGCI with the proposed MPPT control method during the night-time and daytime is discussed in Section VII-D.

A. Comparative Performances of IGCI, CGCI, and HGCI

Figs. 7 and 8 show the performance of the IGCI, CGCI, and HGCI for linear loading and nonlinear loading compensation, in which they are switched ON at 60 ms.

The IGCI, CGCI, and HGCI provide the load required reactive power $Q_{Lxf} = Q_{cxf}$, and inject the active power to its reference value $P_{cxf}{}^* = P_{cxf}$. Based on Fig. 7 and Table III, the IGCI and CGCI require about $V_{\mathrm{DC}} = 300$ V to compensate $Q_{Lxf} = 540$ var and inject $P_{cxf}{}^* = 200$ W to the linear loads power system while the HGCI just requires $V_{\mathrm{DC}} = 100$ V for the same Q_{Lxf} compensation and P_{cxf} injection.

As shown in Fig. 8(a), the IGCI with $V_{\mathrm{DC}} = 300$ V cannot inject the same $P_{cxf}{}^* = 200$ W ($P_{cxf} = 120$ W) when the loads has the harmonic current ($\mathrm{THD}_{isx} = 16.2\%$). However, when V_{DC} increases to 400 V, the IGCI can fully compensate the reactive power and current harmonics problem and inject the $P_{cxf}{}^* = 200$ W as shown in Table III. Based on Fig. 8(b) and (c), the CGCI and HGCI require $V_{\mathrm{DC}} = 300$ and 100 V for fully reactive power ($Q_{cxf} = Q_{Lxf} = 540$ var and current harmonics compensation and also active power injection ($P_{cxf}{}^* = P_{cxf} = 200$ W).

B. EMI Impact of the HGCI

The high switching frequency will introduce high-frequency voltage and current noise components to the system, which is one of the main reasons to cause EMI noise. In order to reduce the EMI noise of the HGCI, the hysteresis PWM method can be used. The operational principle of hysteresis current PWM can spread the energy concentrated around the harmonics of switching frequency to a wider frequency range to reduce the EMI peak value. The following simulation case study is provided to explain the hysteresis PWM control method. From Figs. 9 and 10, it can be seen that the hysteresis PWM method can spread the switching frequency energy in a wider frequency range to reduce the EMI peak value.

Moreover, compared with the conventional high dc-link voltage-controlled IGCIs, the low dc-link voltage characteristic of the HGCI can also help to reduce the EMI noise. The lower

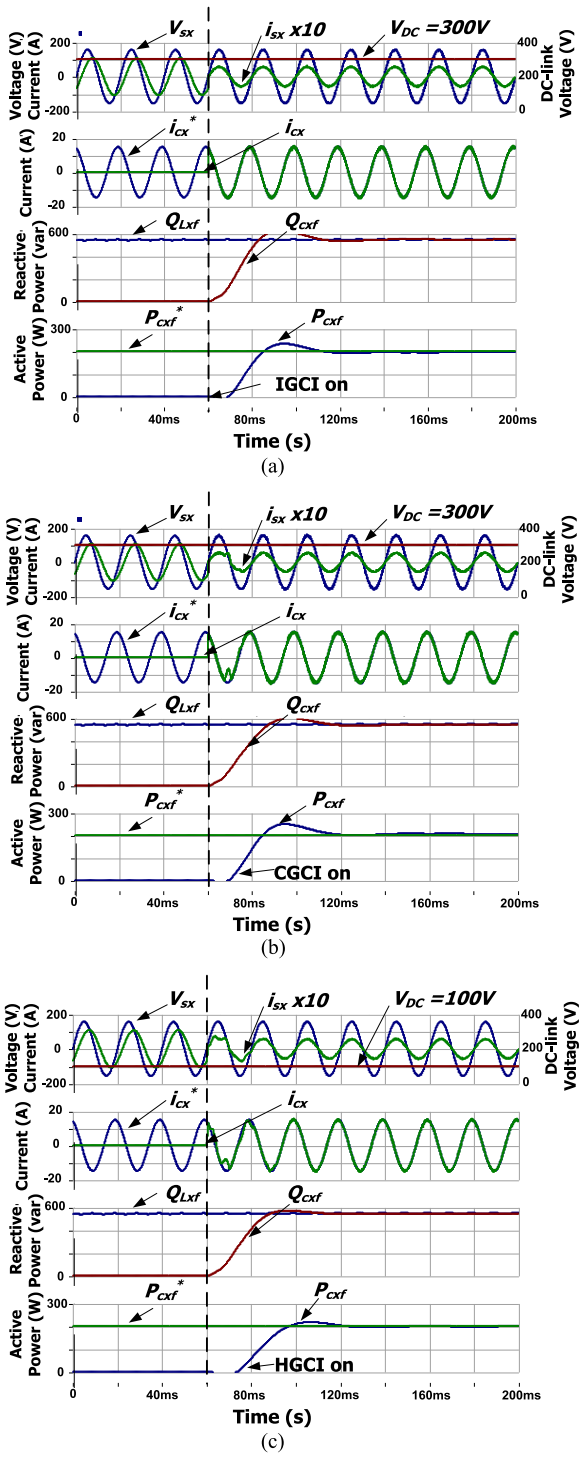

Fig. 7. Simulation results for balanced linear loading compensation before and after: (a) IGCI, (b) CGCI, and (c) HGCI operation.

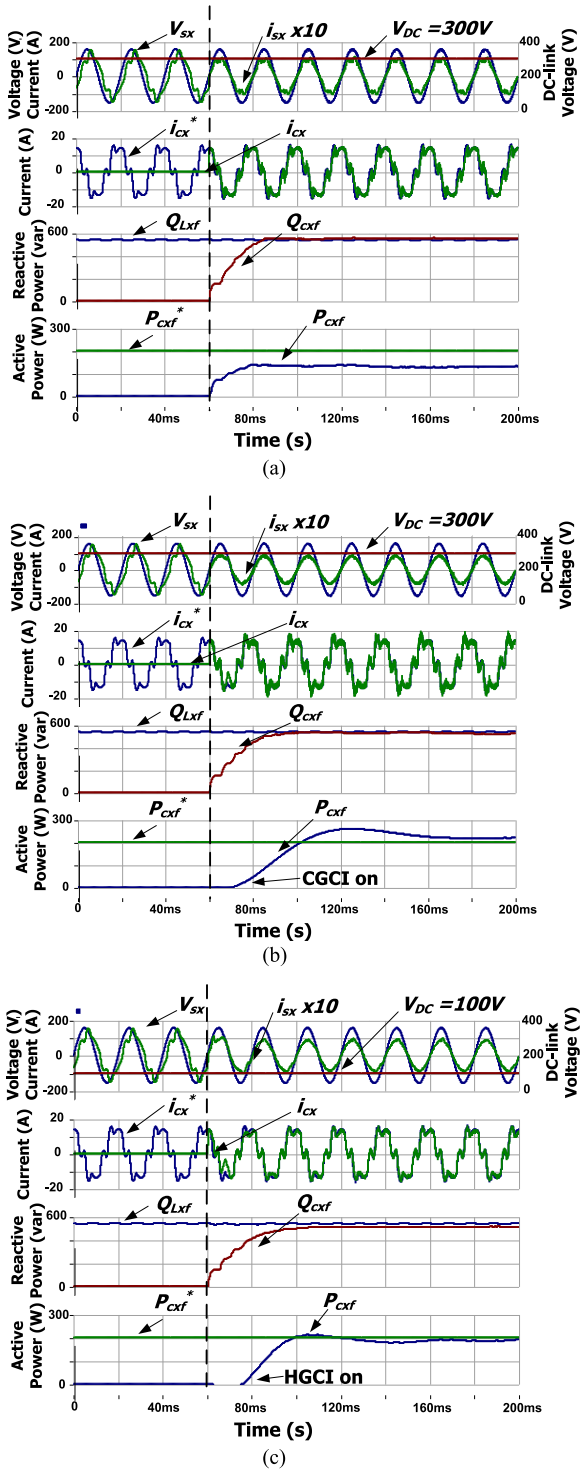

Fig. 8. Simulation results for balanced nonlinear loading compensation before and after: (a) IGCI, (b) CGCI, and (c) HGCI operation.

the dc-link voltage means the lower high-frequency power (voltage). Thus, lowering the high-frequency power (voltage) can lead to the EMI reduction. Besides, the EMI filter for the power supply of the controller, transducers, and drivers of the insulated gate bipolar transistor (IGBT) and thyristors has been installed in the hardware prototype to relax the EMI problem.

C. HGCI for Unbalanced Loads Operation

Fig. 11 shows the performance of the HGCI for unbalanced loads compensation, in which it is switched ON at 80 ms. From Fig. 11 and Table III, by using the HGCI with $V_{\mathrm{DC}} = 100$ V and the proposed control method, the three-phase system source power factors (PFs) have been compensated to unity from the

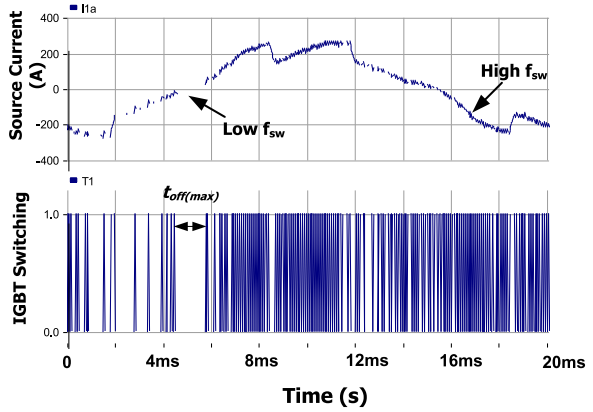

Fig. 9. Waveforms of inverter compensating current and corresponding switching signal of IGBT.

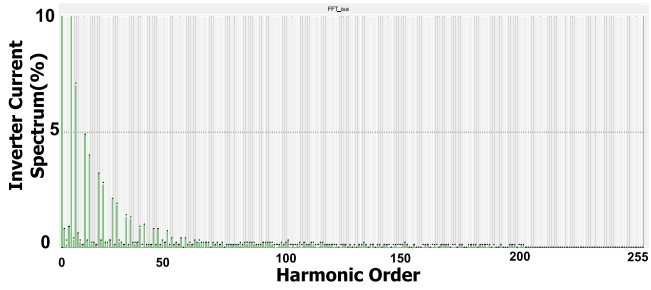

Fig. 10. Spectrum of the inverter compensating current.

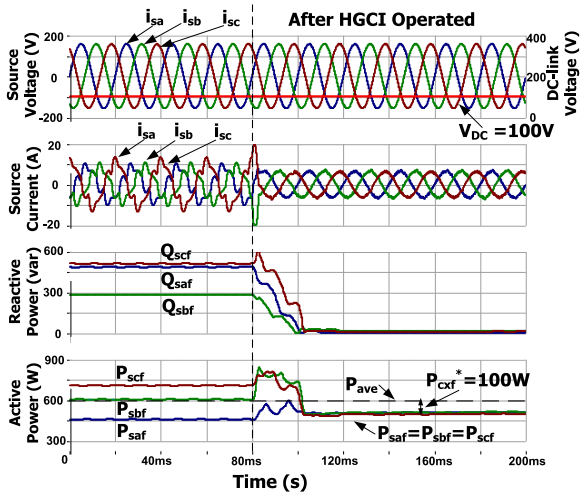

Fig. 11. Simulation results for unbalanced loading compensation before and after HGCI operation.

original 0.68 (showing the worst phase). And, the source reactive powers are compensated close to zero from the original 486, 280, and 508 var. And, the average value of source active power is 591 W (P_{saf} = 457 W, P_{sbf} = 608 W, and P_{scf} = 708 W) before compensation. After compensation, the source active power is balanced to around 498 W with $P_{cxf}{}^{*}$ = 100 W injection for each phase. Moreover, from Table III, the source current THDs are compensated to lower than 5% from 27.4% (showing the worst phase).

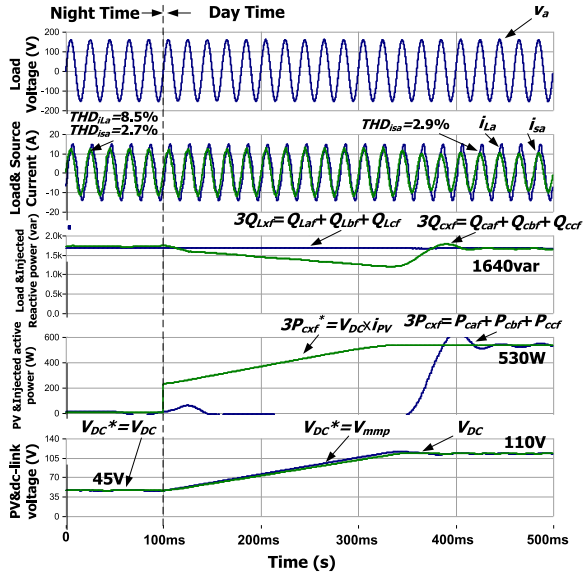

Fig. 12. Simulated waveforms of load voltage, load and source currents, three-phase load and injected reactive powers, PV output and three-phase injected active powers, PV output voltage, and dc-link voltage during HGCI with MPPT control.

D. HGCI With the Proposed MPPT Control Method During Night-Time and Daytime

Fig. 12 illustrates the performance of the HGCI with the proposed MPPT control method during the night-time and daytime. From Fig. 12, it can be seen that the reference dc-link voltage $V_{\mathrm{DC}}{}^{*}$ is keeping at the minimum dc-link voltage reference $V_{\mathrm{DC}m}{}^{*} \approx 45$ V (when $P_{cxf} \approx 0$) during the night-time for harmonic and reactive power compensation. During the daytime, the HGCI can resume its active power injection once the MPPT methods lead to the PV output voltage V_{mmp} higher than its $V_{\mathrm{DC}m}{}^{*} \approx 45$ V. When $V_{\mathrm{mmp}} > V_{\mathrm{DC}m}{}^{*}$, $V_{\mathrm{DC}}{}^{*} = V_{\mathrm{mmp}}$, the HGCI with the PV power is used to inject active power $(P_{cxf}{}^{*} = V_{\mathrm{DC}} \cdot i_{\mathrm{PV}}/3)$ and compensate reactive power, unbalanced power, and harmonics power simultaneously.

From Fig. 12, THD_{isx} has been improved to 2.7% during the night-time and 2.9% during the daytime from the original 8.5%. And, the injected reactive power can fully compensate the load reactive $(Q_{cxf} = Q_{Lxf} = 1640 \text{ var}/3)$ during both night-time and daytime. By using the MPPT method, V_{DC} increases from 45 to about 110 V while the three-phase injected active power increases from zero to 530 W.

VIII. Experimental Results

A three-phase three-wire 110 V–10 A HGCI experimental prototype is designed and constructed in the laboratory as shown in Fig. 13. The digital control system of the HGCI consists of two paralleled digital signal processors (DSPs) TMS320F2812s, and the basic settings of both DSPs are the same. The SanRex PK110FG160 thyristors are used for the TCLC part while the Mitsubishi IGBT intelligent power modules PM300DSA60 are employed as the switching devices of the inverter. Each part of

Fig. 13. Experimental setup of the 110 V–10 A HGCI experimental prototype.

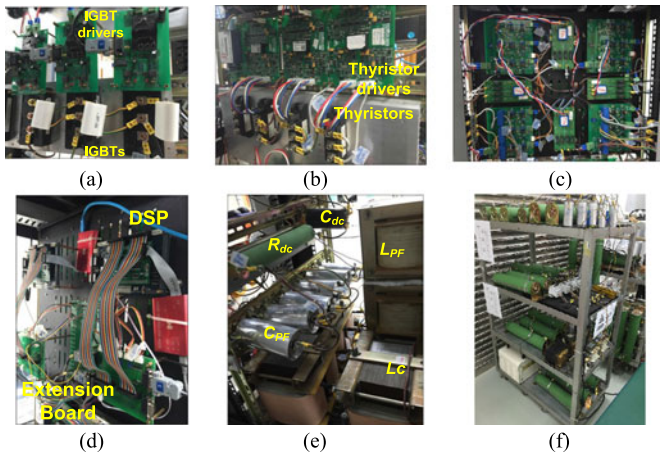

Fig. 14. 110 V–10 A HGCI and loading system: (a) IGBTs and their divers, (b) thyristors and their divers, (c) transducers with signal conditioning circuits, (d) DSPs and their extension boards, (e) TCLC part components, dc capacitor and discharge resistor, and (f) loading system.

the experimental prototype including the testing loads is illustrated in Fig. 14.

The performances of the proposed HGCI for balanced and unbalanced loads compensation are provided in Sections VIII-A and VIII-B. Fig. 15–19 show the waveforms of v_{sx}, i_{sx} Q_{sxf}, and P_{sxf} for balanced and unbalanced reactive power and harmonic current compensation and active power injection by using the HGCI. And Table IV summarizes the experimental results.

A. HGCI for Balanced Loads Compensation

From Fig. 15 and Table IV, it can be seen that the HGCI can compensate THD_{isx} to 9.7% and improve the PF to 0.99 from the original 16.2% and 0.85. And, the voltage THD_{Vx} has been improved from to 4.7% to 3.2% for the worst phase among phases *a, b,* and *c*. As shown in Fig. 16 and Table IV, the

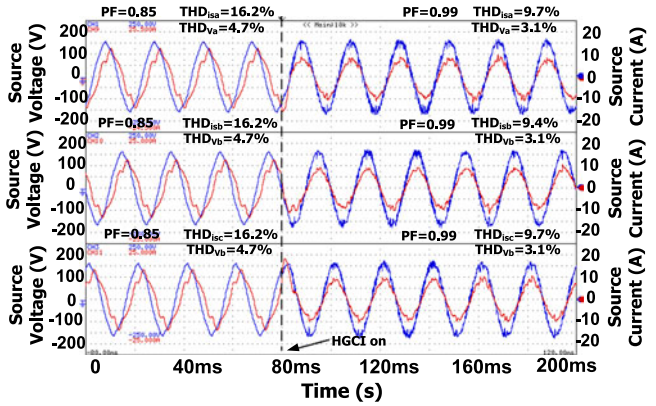

Fig. 15. Waveforms of v_{sx} and i_{sx} for balanced inductive reactive power and harmonic current compensation and active power injection by using the HGCI.

Fig. 16. Dynamic balanced inductive loads compensation by using the HGCI: (a) Q_{sxf} (reactive power compensation) and (b) P_{sxf} (active power injection).

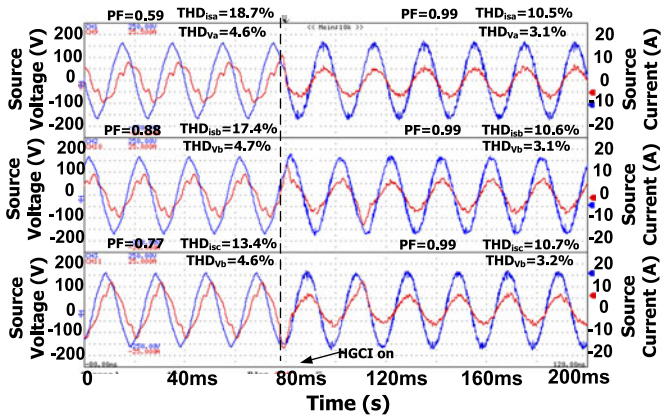

Fig. 17. Waveforms of v_{sx} and i_{sx} for unbalanced inductive reactive power and harmonic current compensation and active power injection by using the HGCI.

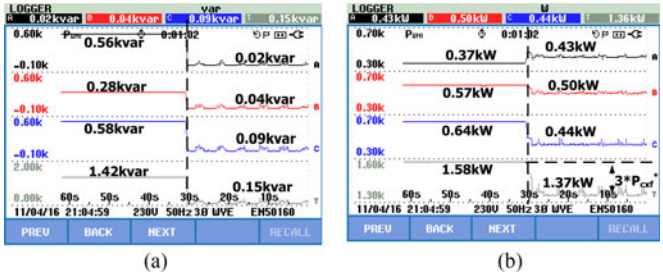

Fig. 18. Dynamic unbalanced inductive loads compensation by using the HGCI: (a) Q_{sxf} (reactive power compensation) and (b) P_{sxf} (active power injection).

TABLE IV
EXPERIMENTAL RESULTS FOR DIFFERENT LOADS COMPENSATION BEFORE AND AFTER THE PROPOSED HGCI COMPENSATION

			I_{sx} (A)	Q_{sx} (var)	P_{sx} (W)	PF	THD_{Vx} (%)	THD_{isx} (%)	V_{DC} (V)
Nonlinear loads (HGCI Comp.)	Before Comp.	A	7.8	0.58k	0.73k	0.85	4.7	16.2	–
		B	7.8	0.58k	0.73k	0.85	4.7	16.2	
		C	7.8	0.58k	0.73k	0.85	4.7	16.2	
	After Comp.	A	4.3	0.05k	0.54k	0.99	3.1	9.7	100
		B	4.3	0.05k	0.55k	0.99	3.1	9.2	
		C	4.3	0.04k	0.54k	0.99	3.1	9.7	
Unbalanced loads (HGCI Comp.)	Before Comp.	A	5.7	0.56k	0.37k	0.59	4.6	18.7	–
		B	5.6	0.28k	0.57k	0.88	4.7	17.4	
		C	7.6	0.58k	0.64k	0.77	4.6	13.4	
	After Comp.	A	4.4	0.02k	0.43k	0.99	3.1	10.5	100
		B	4.8	0.04k	0.50k	0.99	3.1	10.6	
		C	4.4	0.09k	0.44k	0.99	3.2	10.7	

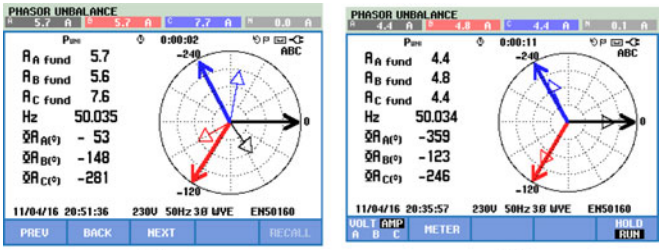

Fig. 19. Experimental phasor diagrams of v_{sx} and i_{sxf} for unbalanced inductive loads: (a) before compensation and (b) after HGCI compensation.

three-phase reactive power has been compensated to 0.14 from 1.74 kvar. With the active power injection function ($P_{cxf}{}^* = 200$ W) during the daytime, the three-phase active power $3P_{sxf}$ has been reduced to 1.63 kW from the original 2.19 kW by using the HGCI.

B. HGCI for Unbalanced Loads Compensation

As shown in Fig. 17 and Table IV, the HGCI can improve the source current THD_{isx} from 18.7% to 10.7% and source voltage THD_{Vx} from 4.7% to 3.2% (showing the worst phase among phases *a, b*, and *c*). And, the worst phase PF is improved from 0.59 to 0.99. From Fig. 18, the HGCI can compensate Q_{sxf} of each phase (0.56, 0.28, and 0.58 kvar) close to zero. And the different P_{sxf} of each phase (0.37, 0.57, and 0.64 kW) has been compensated to approximately the same. Moreover, the total three-phase $3P_{sxf}$ has been reduced to 1.37 kW from the original 1.58 kW. In addition, as shown in Fig. 19, the source voltage and current have been compensated to be in phase with each other for the unbalanced loads compensation.

IX. CONCLUSION

In this paper, the analysis of the structure, parameter design, and control method of a new type dc/ac inverter HGCI for PV power generation with power quality conditioning is proposed. Compared with the conventional IGCI and CGCI, the proposed HGCI has distinct characteristics of wide operational range and low dc-link operating voltage; thus, the system and operational costs can be reduced. Moreover, the HGCI can inject the active power and provide reactive power, unbalanced power, and harmonic power compensation at the same time. Simulation and experimental results are presented to verify the effectiveness and performance of the proposed HGCI, which also shows a much lower dc-link operating voltage than the IGCI and CGCI.

APPENDIX

A. Power Losses of IGCI, CGCI, and HGCI: To compare the power losses of IGCI, CGCI, and HGCI, the experimental results are carried out under 110 V system for power quality compensation of the same loadings in the laboratory. The 1) switching loss and 2) component conduction loss are included in the power losses study. And two different loads are used for measurement. The power losses and compensation results of IGCI, CGCI, and HGCI are summarized in Tables V and VI.

TABLE V
EXPERIMENTAL POWER LOSSES OF IGCI, CGCI, AND HGCI (SWITCHING LOSS AND CONDUCTION LOSS)

	DC-link voltage (V)	First load connected			First and second loads connected		
		Sw. loss (W)	Cond. Loss (W)	Total loss (W)	Sw. loss (W)	Cond. Loss (W)	Total loss (W)
IGCI	340	138	1.2	139.2	162	1.6	163.6
CGCI	105	41	3.2	44.2	59	3.7	62.7
HGCI	60	37.5	5.7	43.2	52.1	7.7	59.8

TABLE VI
EXPERIMENTAL COMPENSATION RESULTS OF IGCI, CGCI, AND HGCI

	DC-link voltage (V)	First load connected		First and second loads connected	
		PF	THD_{isx} (%)	PF	THD_{isx} (%)
Before Comp.	–	0.96	24.5	0.93	12.7
IGCI	340	0.98	9.5	0.99	8.7
CGCI	105	0.85	12.5	0.99	7.5
HGCI	60	0.99	6.3	0.99	5.5

Based on Tables V and VI, it can be seen that IGCI obtains the largest power loss (switching loss and conduction loss) while

the CGCI and HGCI obtain much lower power losses. Besides, HGCI obtains the best compensation results even with the lowest dc-link operating voltage, which shows the advantages of the proposed HGCI.

REFERENCES

[1] Y. P. Siwakoti, F. Z. Peng, F. Blaabjerg, P. C. Loh, and G. E. Town, "Impedance-source networks for electric power conversion Part I: A topological review," *IEEE Trans. Power Electron.*, vol. 30, no. 2, pp. 699–716, Feb. 2015.

[2] P. G. Arul, V. K. Ramachandaramurthy, and R. K. Rajkumar, "Control strategies for a hybrid renewable energy system: A review," *Renewable Sustain. Energy Rev.*, vol. 42, pp. 597–608, 2015.

[3] W. Li, Y. Gu, H. Luo, W. Cui, X. He, and C. Xia, "Topology review and derivation methodology of single-phase transformerless photovoltaic inverters for leakage current suppression," *IEEE Trans. Ind. Electron.*, vol. 62, no. 7, pp. 4537–4551, Jul. 2015.

[4] R. Carbone and A. Tomaselli, "Recent advances on ac PV-modules for grid-connected phtotvoltaic plants," in *Proc. Int. Conf. Clean Electr. Power*, Jun. 2011, pp. 124–129.

[5] F. Rong, X. Gong, and H. Shoudao, "A novel grid-connected PV system based on MMC to get the maximum power under partial shading conditions," *IEEE Trans. Power Electron.*, vol. 32, no. 6, pp. 4320–4333, Jun. 2017, doi: 10.1109/TPEL.2016.2594078.

[6] X. Li, S. Dusmez, U. R. Prasanna, B. Akin, and K. Rajashekara, "A new SVPWM modulated input switched multilevel converter for grid-connected PV energy generation systems," *IEEE J. Emerg. Sel. Topics Power Electron.*, vol. 2, no. 4, pp. 920–930, Dec. 2014.

[7] N. Kumar, T. K. Saha, and J. Dey, "Sliding-mode control of PWM dual inverter-based grid-connected PV system: Modeling and performance analysis," *IEEE J. Emerg. Sel. Topics Power Electron.*, vol. 4, no. 2, pp. 435–444, Jun. 2016.

[8] A. Pigazo, M. Liserre, R. A. Mastromauro, V. M. Moreno, and A. Dell'Aquila, "Wavelet-based islanding detection in grid-connected PV systems," *IEEE Trans. Ind. Electron.*, vol. 56, no. 11, pp. 4445–4455, Nov. 2009.

[9] A. Sangwongwanich, Y. Yang, and F. Blaabjerg, "A sensorless power reserve control strategy for two-stage grid-connected PV systems," *IEEE Trans. Power Electron.*, vol. 32, no. 11, pp. 8559–8569, Nov. 2017, doi: 10.1109/TPEL.2017.2648890.

[10] F. J. Lin, K. C. Lu, T. H. Ke, B. H. Yang, and Y. R. Chang, "Reactive power control of three-phase grid-connected PV system during grid faults using Takagi–Sugeno–Kang probabilistic fuzzy neural network control," *IEEE Trans. Ind. Electron.*, vol. 62, no. 9, pp. 5516–5528, Sep. 2015.

[11] L. Cao, K. H. Loo, and Y. M. Lai, "Output-impedance shaping of bidirectional DAB dc–dc converter using double-proportional-integral feedback for near-ripple-free dc bus voltage regulation in renewable energy systems," *IEEE Trans. Power Electron.*, vol. 31, no. 3, pp. 2187–2199, Mar. 2016.

[12] Y. Bae, T. K. Vu, and R. Y. Kim, "Implemental control strategy for grid stabilization of grid-connected PV system based on German grid code in symmetrical low-to-medium voltage network," *IEEE Trans. Energy Convers.*, vol. 28, no. 3, pp. 619–631, Sep. 2013.

[13] B. N. Alajmi, K. H. Ahmed, G. P. Adam, and B. W. Williams, "Single-phase single-stage transformer less grid-connected PV system," *IEEE Trans. Power Electron.*, vol. 28, no. 6, pp. 2664–2676, Jun. 2013.

[14] H. Choi, M. Ciobotaru, M. Jang, and V. G. Agelidis, "Performance of medium-voltage dc-bus PV system architecture utilizing high-gain dc–dc converter," *IEEE Trans. Sustain. Energy*, vol. 6, no. 2, pp. 464–473, Apr. 2015.

[15] Spatial Distribution of China Average Annual Total Sunshine Hours Between 1978 and 2007, China Meteorological Administration (CMA) Wind and Solar Energy Resource Center. [Online]. Available: http://cwera.cma.gov.cn/ Website/index.php?ChannelID = 121&NewsID = 1985.

[16] T. Ye, N. Dai, C. S. Lam, M. C. Wong, and J. M. Guerrero, "Analysis, design, and implementation of a quasi-proportional-resonant controller for a multifunctional capacitive-coupling grid-connected inverter," *IEEE Trans. Ind. Appl.*, vol. 52, no. 5, pp. 4269–4280, Oct. 2016.

[17] N. Y. Dai, W. C. Zhang, M. C. Wong, J. M. Guerrero, and C. S. Lam, "Analysis, control and experimental verification of a single-phase capacitive-coupling grid-connected inverter," *IET Power Electron.*, vol. 8, no. 5, pp. 770–782, 2015.

[18] C. S. Lam, L. Wang, S. I. Ho, and M. C. Wong, "Adaptive thyristor controlled LC—Hybrid active power filter for reactive power and current harmonics compensation with switching loss reduction," *IEEE Trans. Power Electron.*, vol. 32, no. 10, pp. 7577–7590, Oct. 2017.

[19] L. Wang, C. S. Lam, and M. C. Wong, "Modeling and parameter design of thyristor controlled *LC*-coupled hybrid active power filter (TCLC-HAPF) for unbalanced compensation," *IEEE Trans. Ind. Electron.*, vol. 64, no. 3, pp. 1827–1840, Mar. 2017.

[20] L. Wang, C. S. Lam, and M. C. Wong, "Hardware and software design of a low dc-link voltage and wide compensation range thyristor controlled LC-coupling hybrid active power filter," in *Proc. TENCON 2015 IEEE Region 10 Conf.*, Nov. 2015, pp. 1–4.

[21] L. Wang, C. S. Lam, and M. C. Wong, "An unbalanced control strategy for a thyristor controlled LC-coupling hybrid active power filter (TCLC-HAPF) in three-phase three-wire systems," *IEEE Trans. Power Electron.*, vol. 32, no. 2, pp. 1056–1069, Feb. 2017.

[22] L. Wang, C. S. Lam, and M. C. Wong, "Selective compensation of distortion, unbalanced and reactive power of a thyristor-controlled LC -coupling hybrid active power filter (TCLC-HAPF)," *IEEE Trans. Power Electron.* vol. 32, no. 12, pp. 9065–9077, Dec. 2017.

[23] L. Wang, C. S. Lam, and M. C. Wong, "A Hybrid STATCOM with wide compensation range and low dc-link voltage," *IEEE Trans. Ind. Electron.*, vol. 63, no. 6, pp. 3333–3343, Jun. 2016.

[24] F. Z. Peng and J. S. Lai, "Generalized instantaneous reactive power theory for three-phase power systems," *IEEE Trans. Instrum. Meas.*, vol. 45, no. 1, pp. 293–297, Feb. 1996.

[25] H. Akagi, Y. Kanazawa, and A. Nabae, "Instantaneous reactive power compensators comprising switching devices without energy storage components," *IEEE Trans. Ind. Appl.*, vol. IA-20, no. 3, pp. 625–630, May 1984.

[26] W.-H. Choi, C.-S. Lam, M.-C. Wong, and Y.-D. Han, "Analysis of dc link voltage controls in three-phase four-wire hybrid active power filters," *IEEE Trans. Power Electron.*, vol. 28, no. 5, pp. 2180–2191, May 2013.

[27] L. Wang, C. S. Lam, M. C. Wong, N.-Y. Dai, K.-W. Lao, and C.-K. Wong, "Non-linear adaptive hysteresis band PWM control for hybrid active power filters in reducing switching loss," *IET Power Electron.*, vol. 8, no. 11, pp. 2156–2167, Nov. 2015.

[28] C.-S. Lam, W.-H. Choi, M.-C. Wong, and Y.-D. Han, "Adaptive dc-link voltage controlled hybrid active power filters for reactive power compensation," *IEEE Trans. Power Electron.*, vol. 27, no. 4, pp. 1758–1772, Apr. 2012.

Lei Wang received the B.Sc. degree in electrical and electronics engineering from the University of Macau (UM), Macao, China, in 2011, the M.Sc. degree in electronics engineering from The Hong Kong University of Science and Technology, Clear Water Bay, Hong Kong, in 2012, and the Ph.D. degree in electrical and computer engineering from UM, Macao, China, in 2017.

Currently, he is a Postdoctoral Fellow in the Power Electronics Laboratory, UM. His research interests include power electronics, power quality, distribution flexible ac transmission system, power quality compensation, and renewable energy.

Dr. Wang received the champion award in the "Schneider Electric Energy Efficiency Cup," Hong Kong, 2011.

Chi-Seng Lam (S'04–M'12–SM'16) received the B.Sc., M.Sc., and Ph.D. degrees in electrical and electronics engineering from the University of Macau (UM), Macao, China, in 2003, 2006, and 2012, respectively.

From 2006 to 2009, he was an E&M Engineer with UM. In 2009, he simultaneously worked as a Laboratory Technician and started to work toward the Ph.D. degree, and completed his Ph.D. degree within 3 years. In 2013, he was a Postdoctoral Fellow with The Hong Kong Polytechnic University, Hung Hom, Hong Kong. He is currently an Assistant Professor in the State Key Laboratory of Analog and Mixed-Signal VLSI, UM. He has co-authored 2 books: *Design and Control of Hybrid Active Power Filters* (Springer, 2014) and *Parallel Power Electronics Filters in Three-phase Four-Wire Systems - Principle, Control and Design* (Springer, 2016), 2 US patent, 2 Chinese patents, and more than 60 technical journals and conference papers. His research interests include integrated power electronics controllers, power management integrated circuits, power quality compensators, smart grid technology, renewable energy, etc.

Dr. Lam was the GOLD Officer, a Student Branch Officer, and a Secretary of IEEE Macau Section in 2007, 2008, and 2015. He is currently the Vice-Chair of IEEE Macau Section, the Chair of IEEE Macau CAS/COM Joint Chapter, and the Secretary of IEEE Macau PES/PELS Joint Chapter. He served as a member of Organizing Committee or Technical Program Committee of several international conferences, such as IEEE TENCON 2015, ASP-DAC 2016, etc. He received the Macao Science and Technology Invention Award (Third-Class) and the R&D Award for Postgraduates (Ph.D.) in 2014 and 2012, respectively. He also received Macao Government Ph.D. Research Scholarship in 2009–2012, Macao Foundation Postgraduate Research Scholarship in 2003–2005, and the third RIUPEEEC Merit Paper Award in 2005.

Man-Chung Wong (SM'06) received the B.Sc. and M.Sc. degrees in electrical and electronics engineering from the University of Macau (UM), Macao, China, in 1993 and 1997, respectively, and the Ph.D. degree in electrical engineering from Tsinghua University, Beijing, China, in 2003.

He was a Visiting Fellow with Cambridge University, Cambridge, U.K., in 2014. He is currently an Associate Professor in the Department of Electrical and Computer Engineering, UM. He has co-authored 2 Springer books, more than 100 journal and conference papers, and 8 patents (China and USA). His research interests include power electronics converters, pulse with modulation, active power filters, hybrid active power filters, and hybrid power quality compensator for a high-speed railway power supply system. Recently, an industrial power filter platform was developed and installed in a practical power system based on his research results.

Dr. Wong was a member of several conference committees and the General Chair of IEEE TENCON 2015 Macau. He is with IEEE Macau Section and IEEE Macau Power Joint Chapter for many years. In 2014–2015, he was the Chair of IEEE Macau Section. Currently, he is North Representative of IEEE Region 10 Power and Energy Society and the Chair of IEEE Macau PES/PELS Joint Chapter. He received the Macao Young Scientific Award from Macau International Research Institute in 2000, the Young Scholar Award of UM in 2001, Second Prize for Tsinghua University Excellent Ph.D. Thesis Award in 2003, and the Macao Science and Technology Invention Award (Third-Class) in 2012 and 2014. He supervised several students to receive merit paper awards in conferences and champions in student project competitions.